CERN – EUROPEAN ORGANIZATION FOR NUCLEAR RESEARCH

CLIC – Note – 1172

NOVEL OPEN CAVITY DESIGN FOR ROTATING MODE SLED-TYPE RF PULSE COMPRESSORS

Xiaowei Wu and Alexej Grudiev

CERN, Geneva, Switzerland

CERN-ACC-2021-0004
15/07/2021

Abstract

A new X-band high-power rotating mode SLAC Energy Doubler (SLED)-type rf pulse compressor is proposed. It is based on a novel cavity type, a single open bowl-shaped energy storage cavity with high quality factor and compact size, which is coupled to the waveguide using a compact rotating mode launcher. The novel cavity type is applied to the rf pulse compression system of the main linac rf module of the klystron-based option of the Compact Linear Collider (CLIC). Quasi-spherical rotating modes of $TE_{1,2,4}$ and $TE_{1,2,13}$ are proposed for the correction cavity and storage cavity of the rf pulse compression system respectively. The storage cavity working at $TE_{1,2,13}$ has a quality factor of 240000 and a diameter less than 33 cm. The design of the pulse compressor and in particular of the high-Q cavity will be presented in detail.

Geneva, Switzerland
15 July 2021

Novel open cavity design for rotating mode SLED-type rf pulse compressors

Xiaowei Wu* and Alexej Grudiev
European Organization for Nuclear Research (CERN), Geneva, Switzerland
(Dated: July 15, 2021)

A new X-band high-power rotating mode SLAC Energy Doubler (SLED)-type rf pulse compressor is proposed. It is based on a novel cavity type, a single open bowl-shaped energy storage cavity with high quality factor and compact size, which is coupled to the waveguide using a compact rotating mode launcher. The novel cavity type is applied to the rf pulse compression system of the main linac rf module of the klystron-based option of the Compact Linear Collider (CLIC). Quasi-spherical rotating modes of $TE_{1,2,4}$ and $TE_{1,2,13}$ are proposed for the correction cavity and storage cavity of the rf pulse compression system respectively. The storage cavity working at $TE_{1,2,13}$ has a quality factor of 240000 and a diameter less than 33 cm. The design of the pulse compressor and in particular of the high-Q cavity will be presented in detail.

I. INTRODUCTION

As an alternative to the original two beam Compact Linear Collider (CLIC) concept, the klystron-based CLIC option is considered for the 380 GeV initial energy stage [1]. An X-band rf pulse compressor with a correction cavity chain was selected as a baseline option for the klystron-based CLIC rf module [2–4]. Rf compression obtains high peak power in exchange for reduced rf pulse length. Pulse compressors have been applied and operated for many decades in many facilities, such as SLAC, SwissFEL, SACLA, and PAL-XFEL [5–8]. The first rf pulse compressor named SLAC Energy Doubler (SLED) was invented in 1974 [9]. The key components of a SLED system include a 3 dB coupler with two 90° apart divided power ports and two high intrinsic quality factor (Q_0) energy storage cavities. Different resonant cavities such as barrel open cavity (BOC), single spherical cavity, and corrugated circular cavity were designed in the past years [10–12].

The parameters of the CLIC accelerating structure had been re-evaluated to improve the accelerator performance [13]. Additionally, the pulse compressor design adopted to the new structure parameters was optimized based on the klystron output [15]. It is suggested that a correction cavity with a Q_0 of 6×10^4 and a storage cavity with a Q_0 of 2.4×10^5 is a good compromise that increases the power gain by 7.5% compared to the initial design: from 3.48 to 3.74. The correction cavity chain is used to produce flattop and increase the efficiency [3]. The scheme, pulse shape, and transmission spectrum of the CLIC pulse compression system are illustrated in Fig. 1. Phase-to-amplitude modulation by using two klystrons could be applied to eliminate the ripples of the output pulse in Fig. 1(b) [3]. A novel compact open bowl-shaped energy storage cavity with high Q_0 is proposed to meet the requirements for both the correction cavity and the storage cavity of CLIC. This novel cavity type with rotating mode could also be applied to other pulse compression systems. This paper describes its principle, design, and technical advances.

* xiaowei.wu@cern.ch

II. BOWL-SHAPED OPEN CAVITY

The novel open cavity has a bowl shape, as shown in Fig. 2. The electrical field of the working mode in the top area of the cavity is very small. Thus the top of the cavity can be kept open. The cavity works in a quasi-spherical rotating mode of $TE_{1,2,i}$ which is a dipole mode. The radial index i is dominated by the cavity radius (R_{cav}). The working mode shown in Fig. 2 is $TE_{1,2,13}$. The Q_0 of $TE_{1,2,13}$ at 12 GHz is around 2.4×10^5. Principally, a larger R_{cav} contributes to a higher radial index which results in a higher quality factor. However, more parasitic modes will appear in the larger cavity. The parasitic modes may have high field on the top area which results in high loss in the open boundary. The coupling from parasitic modes to working modes will impact the performance of the pulse compressor. The frequency separation between working mode and parasitic modes should be kept as large as possible. Otherwise absorption materials such as silicon carbide need to be added to damp such modes. DZ_{cav} and R_{arc} are used to optimize the Q_0 of the working mode and the mode separation between working mode and parasitic modes.

The open boundary will also help us to suppress many parasitic modes. The cavity can be easily machined by lathe due to its symmetric and open shape. No brazing is needed for the cavity body manufacturing. This can reduce the cost of the fabrication and increase the fabrication accuracy. The top of the cavity is connected to the stainless steel flange with pumping port. This will make it easier to pump compared with the spherical pulse compressor.

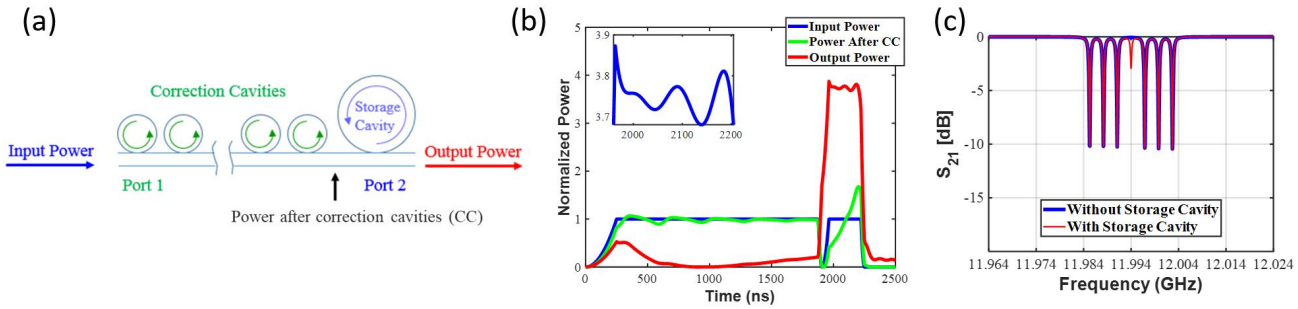

Figure 1: (a) Scheme, (b) pulse shape, and (c) transmission spectrum of the pulse compression system of klystron-based 380 GeV CLIC option. The blue, green, and red curves in (b) are the input power, power after the correction cavity chain, and output power respectively. The quality factor of storage cavity and coupling factor are 2.4×10^5 and 6. The quality factor of correction cavity and coupling factor are 6.0×10^4 and 1.48. Phase-to-amplitude modulation by using two klystrons could be applied to eliminate the ripples of the output pulse [3]. The blue and red curves in (c) are the transmission spectra of the correction cavity chain and the whole system. The frequency difference between two nearby peaks is 2.9 MHz, which corresponds to the pulse length of 344 ns.

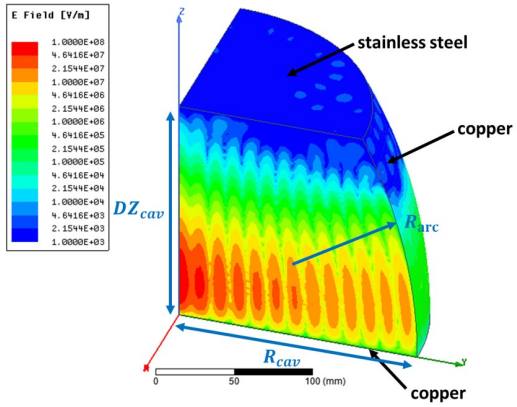

Figure 2: Electrical field of the bowl-shaped open cavity operating at $TE_{1,2,13}$ at 12 GHz. The electrical field is in logarithmic scale.

III. CORRECTION CAVITY DESIGN

A. Cavity design

The Q_0 of the correction cavity is suggested to be 6×10^4 from Ref. [15]. $TE_{1,2,4}$ mode is selected for the bowl-shaped open cavity design with the R_{cav} around 50 mm. The Q_0 is around 75000, which is larger than the requirement. As mentioned in the previous chapter, coupling to the parasitic modes is one of the critical issues in the design. A single cavity model with stainless steel boundary on the top is created to calculate the stainless steel quality factor (Q_{ss}) and the mode frequency separation. Q_{ss} is defined as $\frac{2\pi f W}{P_{ss}}$, where f is the resonant frequency, W is the stored energy, and P_{ss} is the power loss in the stainless steel. The mode spectrum for different R_{arc} is shown in Fig. 3. The middle line with high Q_{ss} is the working mode of $TE_{1,2,4}$ while the other lower Q_{ss} points represent the parasitic modes. R_{arc}=300 mm is selected for the correction cavity design as it has a large mode separation from the nearest two parasitic modes and has a high Q_{ss} value.

B. Coupler design

Though the optimized cavity shape has a large frequency separation between working mode and parasitic modes, the coupling to the parasitic modes may still increase the field at the open area of the cavity after adding the coupling iris. Therefore, the loss in the open boundary area needs to be checked. The coupling iris model is presented in Fig. 4. The top of the cavity model with coupling iris and circular waveguide is set to stainless steel boundary. TE_{11} rotating mode propagates in the circular waveguide and excites $TE_{1,2,4}$ mode in the open cavity via the coupling iris. A quantity named R_{loss} is defined as the ratio between the loss in the stainless steel and that in the copper of the model. The coupling iris is optimized to get the required Q_{ext} and minimum R_{loss}. The minimum R_{loss} of 0.05% is obtained when D_{iris} is 4.44 mm.

The frequencies and quality factors of the working mode and the nearest two parasitic modes are summarized in Table I. The two parasitic modes are around 248.4 MHz and 308.4 MHz away from the working frequency respectively.

The electrical fields of the working mode and the parasitic modes are shown in Fig. 5.

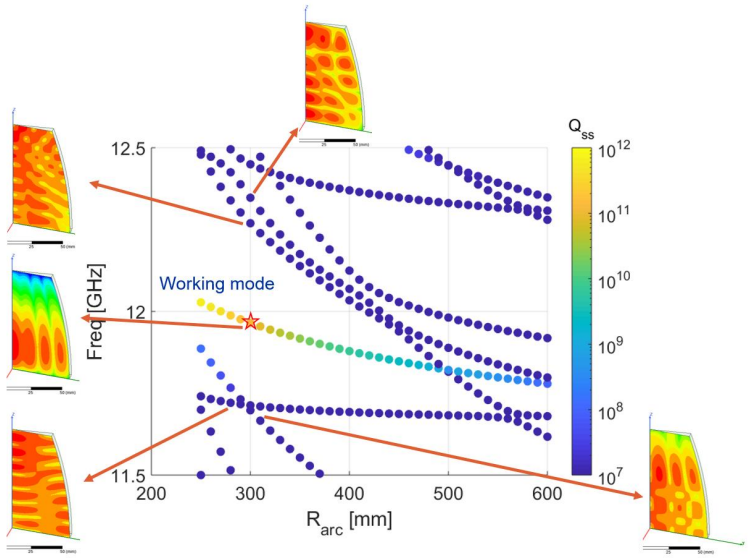

Figure 3: Mode spectrum of $TE_{1,2,4}$ mode cavity. DZ_{cav} is 94.7 mm. R_{cav} is 49.2 mm. Color bar represents the value of Q_{ss}. The electrical fields of the working mode and the parasitic modes are presented in logarithmic scales.

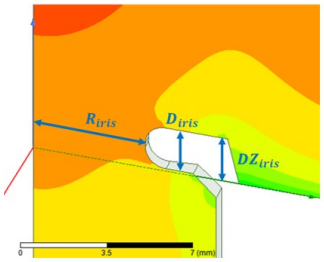

Figure 4: Coupling iris model. The electrical field is in logarithmic scale.

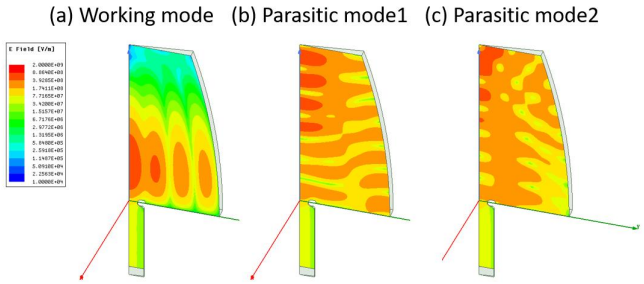

Figure 5: Electrical fields of the working mode and the parasitic modes in the correction cavity. 8 degree slice of the model with a storage energy of 1 J was simulated by the eigenmode solver of HFSS. The electrical fields are in logarithmic scale. (a) is the working mode at 12 GHz. (b) and (c) are the parasitic modes.

Table I: Modes of the correction cavity.

	Frequency [GHz]	Q_0
Working mode	11.994	74659
Parasitic mode1	11.7456	16063
Parasitic mode2	12.3024	14700

C. Frequency domain results

The correction cavity model with coupling iris and circular waveguide was then simulated in the frequency domain solver of HFSS. The field distribution and S_{11} frequency sweep are presented in Fig. 6.

The coupling iris between the circular waveguide and correction cavity was carefully studied and optimized to reduce the rf pulse heating. The final iris has a thickness of 4 mm and a rounding radius of 1.95 mm. As shown in Fig. 1(c), there is a frequency difference between the correction cavity and the rf signal. The resonant frequency, maximum surface electrical field, maximum surface magnetic field, and maximum modified poynting factor (S_c) [16] at the coulping iris of the six correction cavities are presented in Table II. The six correction cavities have different resonant frequencies. The fields in the table are calculated at the input power of 50 MW at steady-state in 11.994 GHz.

D. Tolerance study

The frequencies of the working mode and the parasitic modes are mostly determined by the geometric parameters. Micrometre mechanical tolerances have been achieved using ultra-precision diamond machining [17, 18]. The analysis of the frequency sensitivity of the working mode and the nearest two parasitic modes

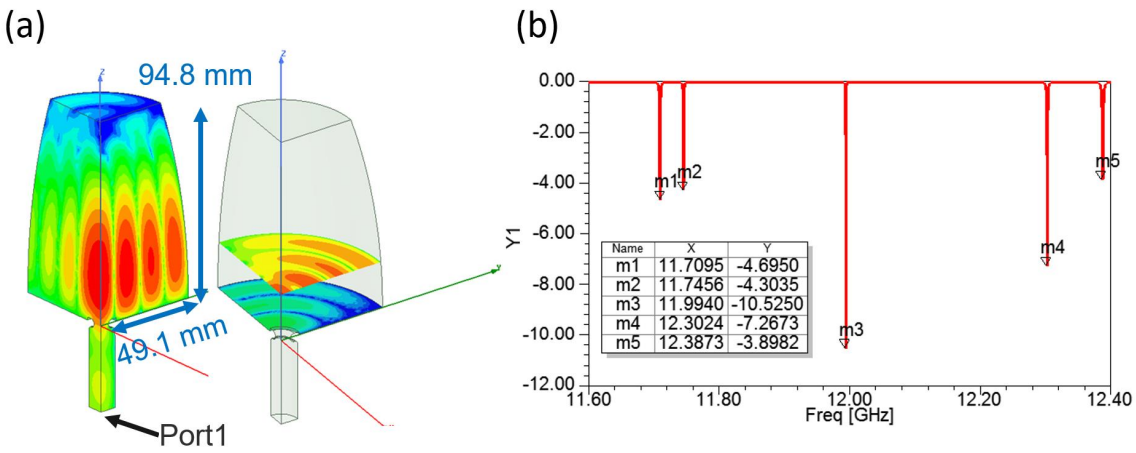

Figure 6: (a) Electrical field of one quarter model of the correction cavity. One quarter model was simulated by the frequency domain solver of HFSS. The electrical field is in logarithmic scale. (b) S_{11} frequency sweep of the correction cavity.

Table II: Rf parameters of the correction cavities.

Frequency [GHz]	E_{max} [MV/m]	H_{max} [kA/m]	S_c [MW/mm^2]
11.9853	11.1	82.43	0.041
11.9882	10.4	78.01	0.037
11.9911	8.26	65.89	0.027
11.9969	17.8	125.8	0.095
11.9998	15.0	107.0	0.069
12.0027	14.1	101.4	0.062

were performed in HFSS, as presented in tables III to VI and summarized in Table VII. It can be concluded that the most critical geometric parameter to the resonant frequency of the working mode is the radius of the cavity (R_{cav}), so that the geometric tolerances are dominated by R_{cav}. The frequency changes of the parasitic modes caused by the machining errors on the geometry is negligible as the two parasitic modes are more than 200 MHz away from the working mode.

Table III: Frequency sensitivity to R_{cav} of the correction cavity.

ΔR_{cav} [mm]	Δf [MHz]		
	Work mode	Parasitic mode1	Parasitic mode2
-0.05	11.9545	2.5485	5.9633
-0.01	2.4032	0.5290	1.2354
-0.005	1.1968	0.2518	0.6010
+0.005	-1.1993	-0.2598	-0.6302
+0.01	-2.3575	-0.4857	-1.1643
+0.05	-11.8905	-2.5149	-5.9788

Table IV: Frequency sensitivity to DZ_{cav} of the correction cavity.

ΔDZ_{cav} [mm]	Δf [MHz]		
	Work mode	Parasitic mode1	Parasitic mode2
-0.05	$< \pm 0.1$	4.8864	2.9254
-0.01	$< \pm 0.1$	0.9746	0.5582
-0.005	$< \pm 0.1$	0.4978	0.2858
+0.005	$< \pm 0.1$	-0.4959	-0.3116
+0.01	$< \pm 0.1$	-0.9962	-0.5639
+0.05	$< \pm 0.1$	-4.7942	-2.8866

Table V: Frequency sensitivity to R_{arc} of the correction cavity.

ΔR_{arc} [mm]	Δf [MHz]		
	Work mode	Parasitic mode1	Parasitic mode2
-0.10	0.1447	$< \pm 0.1$	0.3128
-0.05	$< \pm 0.1$	$< \pm 0.1$	0.1766
-0.01	$< \pm 0.1$	$< \pm 0.1$	$< \pm 0.1$
-0.005	$< \pm 0.1$	$< \pm 0.1$	$< \pm 0.1$
+0.005	$< \pm 0.1$	$< \pm 0.1$	$< \pm 0.1$
+0.01	$< \pm 0.1$	$< \pm 0.1$	$< \pm 0.1$
+0.05	$< \pm 0.1$	$< \pm 0.1$	-0.2038
+0.10	-0.1324	$< \pm 0.1$	-0.3475

E. Model with E-rotator

The so-called E-rotator is used as 3 dB coupler for the SLED system of the bowl-shaped open cavity. It is an rf device with two rectangular and one circular waveguide ports, as shown in Fig. 7. If the input signal comes to the rectangular port 1, the output mode is a right-circularly-polarized TE_{11} mode, as shown in Fig. 7 (a). If the input signal comes to port 2, a left-circularly-polarized

Table VI: Frequency sensitivity to R_{iris} of the correction cavity.

ΔR_{iris} [mm]	Δf [MHz]		
	Work mode	Parasitic mode1	Parasitic mode2
-0.10	0.3549	0.2989	0.3656
-0.05	0.1765	0.1506	0.1716
-0.01	$< \pm 0.1$	$< \pm 0.1$	$< \pm 0.1$
-0.005	$< \pm 0.1$	$< \pm 0.1$	$< \pm 0.1$
+0.005	$< \pm 0.1$	$< \pm 0.1$	$< \pm 0.1$
+0.01	$< \pm 0.1$	$< \pm 0.1$	$< \pm 0.1$
+0.05	-0.1702	-0.1434	-0.1809
+0.10	-0.3169	-0.2597	-0.3323

Table VII: Frequency sensitivity to different geometric parameters of the working mode and the parasitic modes of the correction cavity.

Dimension x	$\Delta f/\Delta$x [MHz/mm]		
	Work mode	Parasitic mode1	Parasitic mode2
R_{cav}	-238.4460	-50.6427	-119.4770
DZ_{cav}	-	-96.8967	-58.0586
R_{arc}	-1.3854	-	-3.4315
R_{iris}	-3.3809	-2.8225	-3.4968

TE_{11} mode is formed, as shown in Fig. 7 (b) [19, 20]. A similar device with the same functionality but different design concept, an rf polarizer, is described in Ref. [21].

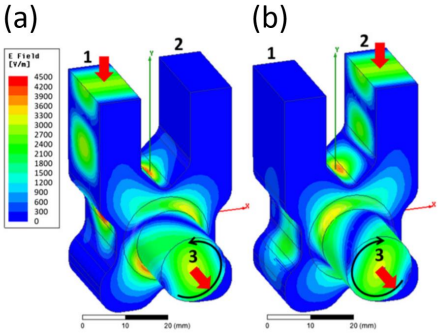

Figure 7: E-rotator geometry and electric field distribution for 1 W of input power into port 1 (a) and port 2 (b). The polarization of the circular TE_{11} mode in the output port is indicated using black arrows [20].

The electrical field distribution of the correction cavity with the E-rotator is shown in Fig. 8. The S_{12} frequency sweep of the correction cavity system is shown in Fig. 9.

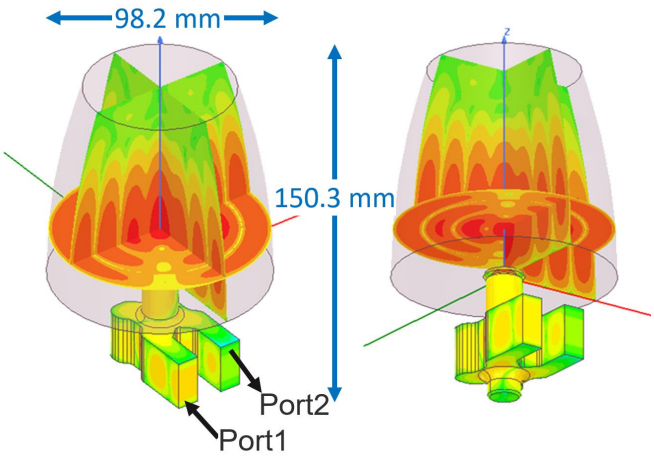

Figure 8: Electrical field distribution of the correction cavity with the E-rotator. The electrical field is in logarithmic scale.

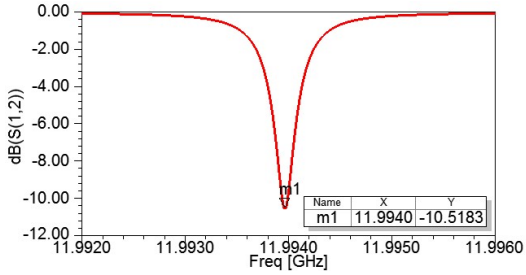

Figure 9: S_{12} frequency sweep of the correction cavity system.

IV. STORAGE CAVITY DESIGN

A. Cavity design

The Q_0 of the storage cavity is suggested to be 2.4×10^5 from Ref. [15]. $TE_{1,2,13}$ mode is selected for the bowl-shaped open cavity design with a cavity radius around 163 mm. The Q_0 is around 240000. The mode spectrum of the storage cavity for different R_{arc} is shown in Fig. 10. The middle line with high Q_{ss} is the working mode of $TE_{1,2,13}$ while the other lower Q_{ss} points represent the parasitic modes. R_{arc}=460 mm is selected for the storage cavity design as it has a high Q_{ss} value and a large mode separation from the nearest two parasitic modes.

B. Coupler design

As with the design of the correction cavity, the loss in the open boundary area is checked in the coupling iris design. The minimum R_{loss} of 1.4% is obtained when the coupling iris radius is 5.21 mm. However, the frequency separation between working mode and parasitic modes

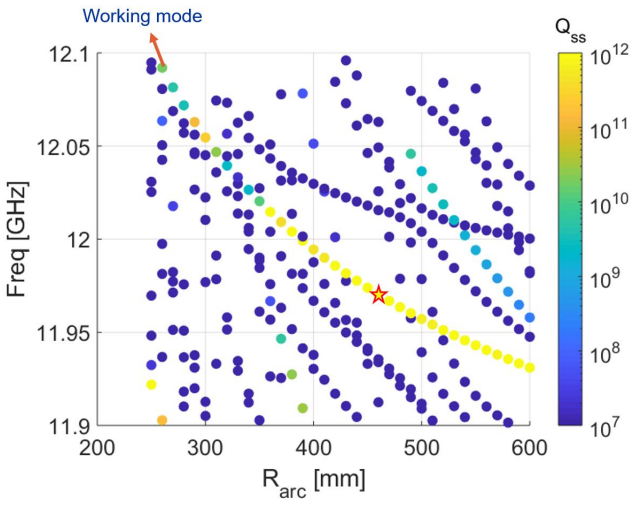

Figure 10: Mode spectrum of $TE_{1,2,13}$ mode cavity. $DZ_{\rm cav}$ is 170 mm. $R_{\rm cav}$ is 163.6 mm. Color bar represents the value of $Q_{\rm ss}$.

is smaller than that of the correction cavity, as shown in Table VIII. The nearest two parasitic modes are 30.5 MHz and 45.9 MHz away from the working frequency respectively.

Table VIII: Modes of the storage cavity.

	Frequency [GHz]	Q_0
Working mode	11.994	244542
Parasitic mode1	11.9635	51431
Parasitic mode2	12.0399	61012

The electrical fields of the working mode and the parasitic modes are shown in Fig. 11.

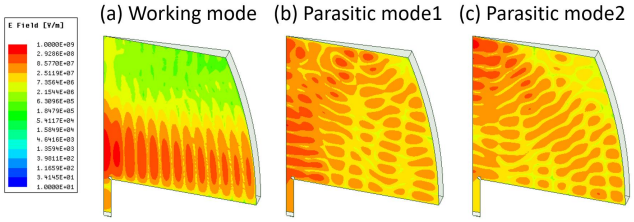

Figure 11: Electrical field of the working mode and the parasitic modes in the storage cavity. 8 degree slice of the model with a storage energy of 1 J was simulated by the eigenmode solver of HFSS. The electrical fields are in logarithmic scale. (a) is the working mode at 12 GHz. (b) and (c) are the parasitic modes.

C. Frequency Domain results

The field distribution and S_{11} frequency sweep are presented in Fig. 12.

The coupling iris between the circular waveguide and storage cavity was carefully studied and optimized to reduce the rf pulse heating. The final iris has a thickness of 3 mm and a rounding radius of 1.485 mm. The resonant frequency, maximum surface electrical field, maximum surface magnetic field, and maximum modified poynting factor ($S_{\rm c}$) [16] at the coulping iris of the storage cavity are presented in Table IX. The field in the table are calculated at an input power of 50 MW at steady state.

Table IX: Rf parameters of the storage cavity.

Frequency [GHz]	$E_{\rm max}$ [MV/m]	$H_{\rm max}$ [kA/m]	$S_{\rm c}$ [MW/mm^2]
11.994	97.79	577.0	2.4606

As the maximum surface magnetic field of storage cavity is higher than that of correction cavities shown in Table I, the temperature rise of storage cavity was calculated at the nominal input pulse. The pulse after the correction cavity chain, compressed pulse with an 2250 ns, 50 MW input pulse, the temperature rise, and the stored energy are shown in Fig. 13. The temperature rise of one point on surface can be calculated as [22]

$$\Delta T(t) = \frac{1}{\sqrt{\pi k \rho c_\varepsilon}} \int_0^t \frac{R_s |H(t')|^2}{2\sqrt{t-t'}} dt', \qquad (1)$$

where $k = 391$ W/(m·K) is the thermal conductivity, $\rho = 8.95 \times 10^3$ kg/m^3 is the density, and $c_\varepsilon = 385$ J/(kg·K) is the specific heat capacity. $R_s = \sqrt{\pi \mu_0 f \rho_{res}}$ and $\rho_{res} = 1.7 \times 10^{-8}$ Ω·m are the electric resistivities. The square of the maximum surface magnetic field $|H_{\rm max}(t)|^2$ is proportional to the stored energy $W(t)$ in a resonant cavity. The stored energy in the bowl-shaped open cavity can be derived from the input and output power according to [9]

$${E_{\rm k}}^2 = (E_{\rm e} + E_{\rm k})^2 + \frac{{E_{\rm e}}^2}{\beta} + \frac{2Q_0 E_{\rm e}}{\omega_0 \beta} \frac{dE_{\rm e}}{dt}, \qquad (2)$$

where $E_{\rm k}$ is the incident electrical field from the rf source, $E_{\rm e}$ is the eletrcical field emitted from the resonant cavity, and the loaded field is $E_{\rm l} = E_{\rm k} + E_{\rm e}$. ω_0 is the angular resonant frequency, β is the coupling factor, and Q_0 is the unloaded quality factor. Thus, the maximum surface magnetic field can be expressed as

$$|H_{\rm max}(t)|^2 = C_0 W(t), \qquad (3)$$

$$W(t) = \frac{Q_0}{2\pi\beta f} \left(\sqrt{P_{\rm out}(t)} - \sqrt{P_{\rm in}(t)} \right)^2, \qquad (4)$$

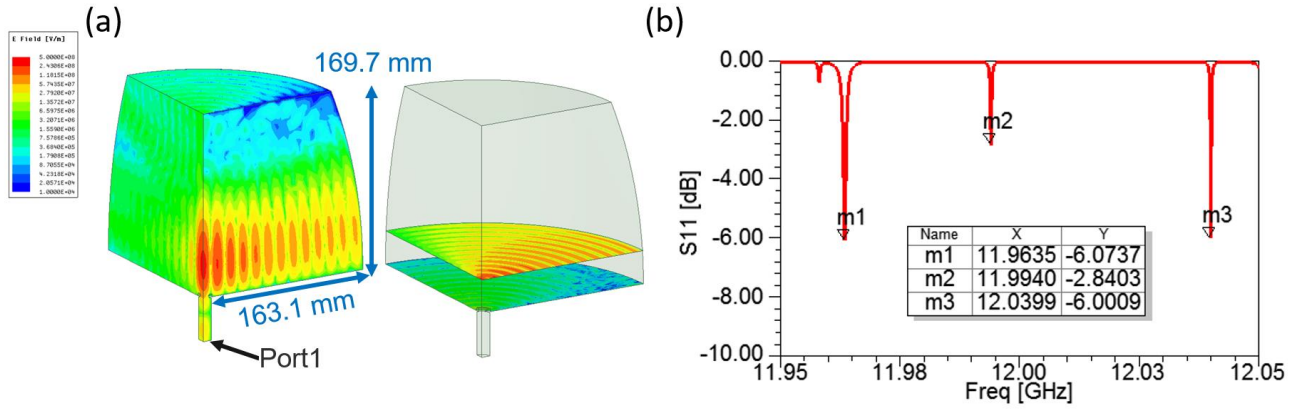

Figure 12: (a) Electrical field of one quarter model of storage cavity. One quarter model was simulated by frequency domain solver of HFSS. The electrical field is in logarithmic scale. (b) S_{11} frequency sweep of the storage cavity.

where f is the resonant frequency, P_{out} is the output power, P_{in} is the input power, and $C_0 = 91.5 \times 10^{11}$ A^2/(m^2·J) was calculated from the eigenmode solver of HFSS. The maximum temperature rise of the storage cavity is 93.8 K at 50 MW, 2250 ns input pulse, as shown in Fig. 13. The temperature rise is higher than that of CLIC accelerating structures at nominal power. A compact X-band pulse compressor described in Ref [12] consists of a corrugated cylindrical cavity for energy storage and an rf polarizer which has same functionality as E-rotator to direct the power flow. Similar to the bowl-shaped open cavity, high surface field is located in the iris region. The high-power tests indicated that a breakdown rate of 8.34×10^{-6} 1/pulse was observed at the pulse heating of 658 K. It is speculated that bowl-shaped open cavity can work at low-breakdown rate regime because the pulse heating at iris is less than 100 K based on the reported experimental data.

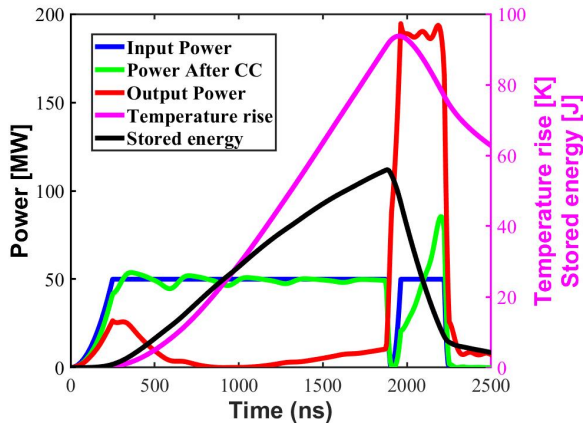

Figure 13: The blue, green, red, pink, and black curves are the input power, power after the correction cavity chain, output power, temperature rise, and stored energy respectively. The quality factor of storage cavity and coupling factor are 2.45×10^5 and 6.11. The quality factor of correction cavity and coupling factor are 7.47×10^4 and 1.84.

D. Tolerance study

The analysis of the frequency sensitivity of the working mode and the nearest two parasitic modes were performed in HFSS, as presented in tables X to XIII and summarized in Table XIV. It can be concluded that the most critical geometric parameter to the resonant frequency of the working mode is the radius of the cavity (R_{cav}), so that the geometric tolerances are dominated by R_{cav}. Geometrical error of 0.01 mm which is rather large compared to what can be achieved with modern Ultra high precision turning machines results in the frequency error of 1 MHz which is much smaller than the frequency separation between the working mode and parasitic modes. This give us strong confidence that the mode separation will not be significantly affected by geometrical errors.

Table X: Frequency sensitivity to D_{cav} of the storage cavity.

ΔD_{cav} [mm]	Δf [MHz]		
	Work mode	Parasitic mode1	Parasitic mode2
-0.05	3.6362	1.2222	1.7004
-0.01	0.7267	0.2450	0.3428
-0.005	0.3643	0.1209	0.1755
+0.005	-0.3608	-0.1165	-0.1628
+0.01	-0.7163	-0.2227	-0.3335
+0.05	-3.632	-1.2238	-1.7075

Table XI: Frequency sensitivity to $DZ_{\rm cav}$ of the storage cavity.

$\Delta DZ_{\rm cav}$ [mm]	Δf [MHz]		
	Work mode	Parasitic mode1	Parasitic mode2
-0.05	$< \pm 0.1$	2.2638	1.8769
-0.01	$< \pm 0.1$	0.4729	0.3930
-0.005	$< \pm 0.1$	0.2322	0.1943
+0.005	$< \pm 0.1$	-0.2321	-0.1914
+0.01	$< \pm 0.1$	-0.4593	-0.3822
+0.05	$< \pm 0.1$	-2.2806	-1.8814

Table XII: Frequency sensitivity to $R_{\rm arc}$ of the storage cavity.

$\Delta R_{\rm arc}$ [mm]	Δf [MHz]		
	Work mode	Parasitic mode1	Parasitic mode2
-0.05	$< \pm 0.1$	$< \pm 0.1$	$< \pm 0.1$
-0.01	$< \pm 0.1$	$< \pm 0.1$	$< \pm 0.1$
-0.005	$< \pm 0.1$	$< \pm 0.1$	$< \pm 0.1$
+0.005	$< \pm 0.1$	$< \pm 0.1$	$< \pm 0.1$
+0.01	$< \pm 0.1$	$< \pm 0.1$	$< \pm 0.1$
+0.05	$< \pm 0.1$	$< \pm 0.1$	$< \pm 0.1$

Table XIII: Frequency sensitivity to $R_{\rm iris}$ of the storage cavity.

$\Delta R_{\rm iris}$ [mm]	Δf [MHz]		
	Work mode	Parasitic mode1	Parasitic mode2
-0.10	$< \pm 0.1$	0.2341	$< \pm 0.1$
-0.05	$< \pm 0.1$	0.1432	$< \pm 0.1$
-0.01	$< \pm 0.1$	$< \pm 0.1$	$< \pm 0.1$
-0.005	$< \pm 0.1$	$< \pm 0.1$	$< \pm 0.1$
+0.005	$< \pm 0.1$	$< \pm 0.1$	$< \pm 0.1$
+0.01	$< \pm 0.1$	$< \pm 0.1$	$< \pm 0.1$
+0.05	$< \pm 0.1$	-0.1214	$< \pm 0.1$
+0.10	$< \pm 0.1$	-0.2430	$< \pm 0.1$

Table XIV: Frequency sensitivity to different geometric parameters of the working mode and the parasitic modes of the storage cavity.

Dimension x	$\Delta f/\Delta$x [MHz/mm]		
	Work mode	Parasitic mode1	Parasitic mode2
$R_{\rm cav}$	-72.6604	-24.4127	-34.0664
$DZ_{\rm cav}$	-	-45.4976	-37.6375
$R_{\rm arc}$	-	-	-
$R_{\rm iris}$	-	-2.4375	-

E. Model with E-rotator

The electrical field distribution of the storage cavity with the E-rotator is shown in Fig. 14. The S_{12} frequency sweep of the storage cavity system is shown in Fig. 15.

Compared with the $\rm TE_{1,2,4}$ mode of the correction cavity, the $\rm TE_{1.2.13}$ mode has smaller mode separation which may cause instability during operation.

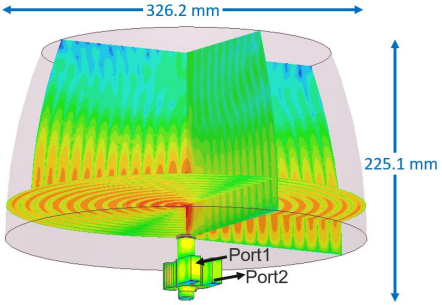

Figure 14: Electrical field distribution of the storage cavity with the E-rotator. The electrical field is in logarithmic scale.

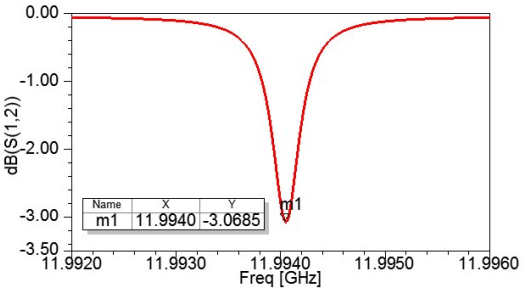

Figure 15: S_{12} frequency sweep of the storage cavity system.

V. CONCLUSION

A new X-band high-power rotating mode SLED-type rf pulse compressor is proposed. It is based on a single open bowl-shaped energy storage cavity working at quasi-spherical rotating mode. It has high Q_0 and compact size. The cavity can be fabricated by lathe with high accuracy due to its symmetric shape. Tolerance study indicates that the frequency shift caused by the machining error can easily compensated by the water temperature. The cavity is coupled to a circular waveguide with a compact rotating mode launcher. An open cavity working at $\rm TE_{1,2,4}$ mode is proposed for the correction cavity design of CLIC rf pulse compression system. It has a Q_0 of 74659 and a diameter less than 5 cm. $\rm TE_{1,2,13}$ mode is proposed for the storage cavity design of CLIC rf pulse compression system. It has a high Q_0 of 244542 and a diameter less than 33 cm.

ACKNOWLEDGMENTS

The authors would like to thank Dr. Igor Syratchev and Dr. Walter Wuensch for their helpful discussions and suggestions on this work.

[1] M. Aicheler, P. Burrows, N. Catalan, R. Corsini, M. Draper, J. Osborne, D. Schulte, S. Stapnes, and M. Stuart, arXiv e-prints , arXiv (2019).

[2] S. Y. Kazakov (1992).

[3] P. Wang, H. Zha, I. Syratchev, J. Shi, and H. Chen, Phys. Rev. Accel. Beams **20**, 112001 (2017).

[4] Y. Jiang, H. Zha, P. Wang, J. Shi, H. Chen, W. L. Millar, and I. Syratchev, Phys. Rev. Accel. Beams **22**, 082001 (2019).

[5] R. Akre, V. Bharadwaj, P. Emma, and P. Krejcik, arXiv preprint physics/0008171 (2000).

[6] T. Schietinger, M. Pedrozzi, M. Aiba, V. Arsov, S. Bettoni, B. Beutner, M. Calvi, P. Craievich, M. Dehler, F. Frei, R. Ganter, C. P. Hauri, R. Ischebeck, Y. Ivanisenko, M. Janousch, M. Kaiser, B. Keil, F. Löhl, G. L. Orlandi, C. Ozkan Loch, P. Peier, E. Prat, J.-Y. Raguin, S. Reiche, T. Schilcher, P. Wiegand, E. Zimoch, D. Anicic, D. Armstrong, M. Baldinger, R. Baldinger, A. Bertrand, K. Bitterli, M. Bopp, H. Brands, H. H. Braun, M. Brönnimann, I. Brunnenkant, P. Chevtsov, J. Chrin, A. Citterio, M. Csatari Divall, M. Dach, A. Dax, R. Ditter, E. Divall, A. Falone, H. Fitze, C. Geiselhart, M. W. Guetg, F. Hämmerli, A. Hauff, M. Heiniger, C. Higgs, W. Hugentobler, S. Hunziker, G. Janser, B. Kalantari, R. Kalt, Y. Kim, W. Koprek, T. Korhonen, R. Krempaska, M. Laznovsky, S. Lehner, F. Le Pimpec, T. Lippuner, H. Lutz, S. Mair, F. Marcellini, G. Marinkovic, R. Menzel, N. Milas, T. Pal, P. Pollet, W. Portmann, A. Rezaeizadeh, S. Ritt, M. Rohrer, M. Schär, L. Schebacher, S. Scherrer, V. Schlott, T. Schmidt, L. Schulz, B. Smit, M. Stadler, B. Steffen, L. Stingelin, W. Sturzenegger, D. M. Treyer, A. Trisorio, W. Tron, C. Vicario, R. Zennaro, and D. Zimoch, Phys. Rev. Accel. Beams **19**, 100702 (2016).

[7] T. Inagaki, C. Kondo, H. Maesaka, T. Ohshima, Y. Otake, T. Sakurai, K. Shirasawa, and T. Shintake, Phys. Rev. ST Accel. Beams **17**, 080702 (2014).

[8] Y. Joo, H.-S. Lee, W. Hwang, Y. Park, K. Oh, and B.-J. Lee, Journal of the Korean Physical Society **63**, 1253 (2013).

[9] Z. D. Farkas, H. A. Hoag, G. A. Loew, and P. B. Wilson, in *9th International Conference on High-Energy Accelerators* (1974).

[10] I. Syrachev, in *Proc. IVth Europ. particle accelerator conference*, Vol. 27 (1994) pp. 375–379.

[11] J. W. Wang, S. G. Tantawi, C. Xu, M. Franzi, P. Krejcik, G. Bowden, S. Condamoor, Y. Ding, V. Dolgashev, J. Eichner, A. Haase, J. R. Lewandowski, and L. Xiao, Phys. Rev. Accel. Beams **20**, 110401 (2017).

[12] Y. Jiang, J. Shi, P. Wang, H. Zha, X. Wu, H. Chen, C. Cheng, and W. Gai, in *8th Int. Particle Accelerator Conf.(IPAC'17), Copenhagen, Denmark, 14â 19 May, 2017* (JACOW, Geneva, Switzerland, 2017) pp. 4214–4217.

[13] J. Liu and A. Grudiev, *RF design of accelerating structure for the main linac of the klystron-based first stage of CLIC at 380 GeV*, CLIC-Note-1082 (CERN, Geneva, 2018).

[15] J. Cai and I. Syratchev, *The design update of the X-band RF pulse compressor with Correction Cavities for the CLIC 380 GeV klystron based accelerator*, CLIC-Note-1166 (CERN, Geneva, 2020).

[16] A. Grudiev, S. Calatroni, and W. Wuensch, Phys. Rev. ST Accel. Beams **12**, 102001 (2009).

[17] J. Liu, J. Shi, A. Grudiev, H. Zha, and H. Chen, Nuclear Instruments and Methods in Physics Research Section A: Accelerators, Spectrometers, Detectors and Associated Equipment **981**, 164499 (2020).

[18] J. Sauza-Bedolla, H. Bursali, N. Catalán Lasheras, A. Grudiev, S. Lebet, E. Rodriguez-Castro, P. Sobrino-Mompean, A. Solodko, and K. Szypula (2018) p. TUPO023. 3 p.

[19] A. Grudiev, *Design of compact high power rf components at x-band*, CLIC-Note-1067 (CERN, Geneva, 2016).

[20] P. Craievich, M. Bopp, H.-H. Braun, A. Citterio, R. Fortunati, R. Ganter, T. Kleeb, F. Marcellini, M. Pedrozzi, E. Prat, S. Reiche, K. Rolli, R. Sieber, A. Grudiev, W. L. Millar, N. Catalan-Lasheras, G. McMonagle, S. Pitman, V. d. P. Romano, K. T. Szypula, W. Wuensch, B. Marchetti, R. Assmann, F. Christie, B. Conrad, R. D'Arcy, M. Foese, P. G. Caminal, M. Hoffmann, M. Huening, R. Jonas, O. Krebs, S. Lederer, D. Marx, J. Osterhoff, M. Reukauff, H. Schlarb, S. Schreiber, G. Tews, M. Vogt, A. d. Z. Wagner, and S. Wesch, Phys. Rev. Accel. Beams **23**, 112001 (2020).

[21] M. Franzi, J. Wang, V. Dolgashev, and S. Tantawi, Phys. Rev. Accel. Beams **19**, 062002 (2016).

[22] D. P. Pritzkau and R. H. Siemann, Phys. Rev. ST Accel. Beams **5**, 112002 (2002).